Observing single-atom catalytic sites during reactions with electrospray ionization mass spectrometry

Max J. Hülsey,[a] Geng Sun,[b,c] Philippe Sautet,[b,c] and Ning Yan*[a]

This contribution is dedicated to Prof. Dr. Maria Flytzani-Stephanopoulos for her pioneering work in catalysis and in particular single-atom catalysis as well as her mentoring to young catalysis researchers.

[1] M. J. Hülsey, Prof. Dr. N. Yan
Department of Chemical and Biomolecular Engineering
National University of Singapore
1 Engineering Drive 3, 117580 Singapore
E-mail: ning.yan@nus.edu.sg
[2] Dr. Geng Sun, Prof. Philippe Sautet
Department of Chemistry and Biochemistry
University of California, Los Angeles
CA, USA
[3] Dr. Geng Sun, Prof. Philippe Sautet
Department of Chemical and Biomolecular Engineering
University of California, Los Angeles
CA, USA

Supporting information for this article is given via a link at the end of the document.

Abstract: Single-atom catalysts (SACs) have become a prominent theme in heterogeneous catalysis, not least because of the potential fundamental insight into active sites. The desired level of understanding, however, is prohibited due to the inhomogeneity of most supported SACs and the lack of suitable tools for structure-activity correlation studies with atomic resolution. Herein, we describe the potency of electrospray ionization mass spectrometry (ESI-MS) to study molecularly defined SACs supported on polyoxometalates in catalytic reactions. We identified the exact composition of active sites and their evolution in the catalytic cycle during CO and alcohol oxidation reactions performed in the liquid phase. Critical information on metal-dependent reaction mechanisms, the key intermediates, the dynamics of active sites and even the stepwise activation barriers were obtained, which would be challenging to gather via prevailingly adopted techniques in SAC research. DFT calculations revealed intricate details of the reaction mechanisms, and strong synergies between ESI-MS defined SAC sites and electronic structure theory calculations become apparent.

Introduction

Single-atom catalysts (SACs) are sometimes superior to their particle counterpart because of enhanced metal dispersion, more variable oxidation states and intimate metal-support interactions.[1] Various combinations of metal and support have been employed for numerous catalytic applications like CO[2] and alcohol oxidation,[3] selective hydrogenation,[4] and electrochemical reactions[5] among others.[1b, 1e, 6] Although parallels are drawn between homogeneous and heterogeneous catalysts,[7] substantial questions remain about SACs regarding: (i) the exact molecular structure of the active site, (ii) the dynamics of that active site under reaction conditions,[8] as well as (iii) activation barriers between various intermediates in the catalytic cycle. Experimental techniques employed so far for model SACs have only been able to provide limited and imprecise information on the active site hampered by their intrinsic constraints. Spectroscopic methods like X-ray photoelectron (XPS), X-ray absorption (XAS) or Mößbauer spectroscopy provide averaged information of observable species, and thus are markedly affected by the presence of spectators. Further, they are element-specific so only provide limited and biased information from the point of view of a particular component of the catalyst.[9] Although state-of-the-art microscopy offers atomic resolution of active sites, changes in the support structure and adsorption of intermediates are difficult to discern. Furthermore, microscopy-based techniques do not allow the acquisition of statistic information of a large number of active sites.[10] Infrared spectroscopy is also commonly used but only offers indirect deductions on the active sites from the perspective of infrared light-responsive surface adsorbates. Those shortcomings highlight the urgent need to develop new methods to interrogate SAC active sites under reaction conditions.

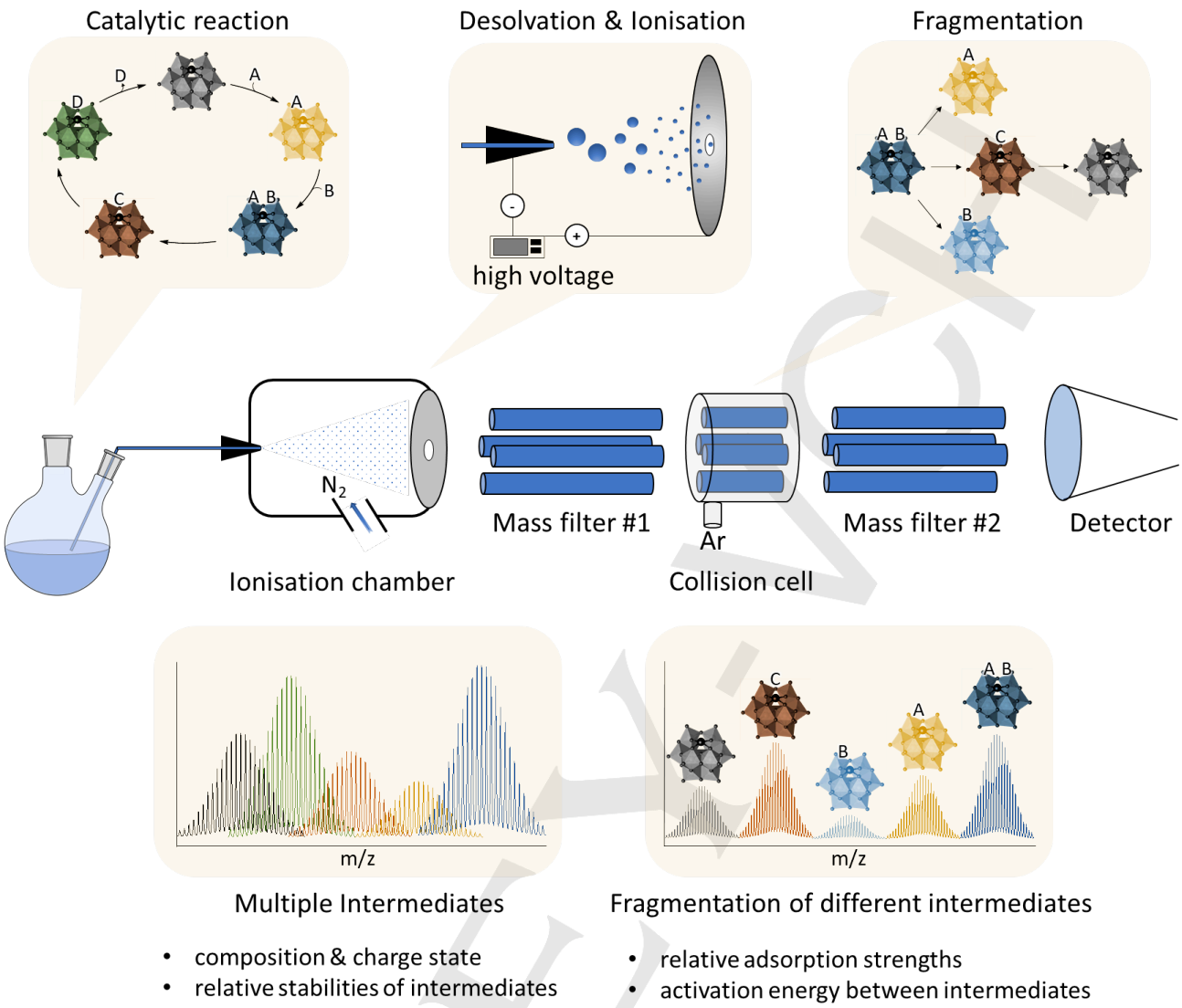

Figure 1. ESI-MS as a tool for the elucidation of single-atom catalysed reaction. Reaction solution including the solubilised SAC, solvents and reaction intermediates is directly injected into the ionisation chamber. The nebulised reaction mixture is heated and accelerated by an electric potential while the solvent droplets are shrinking until the isolated ions are in the gas phase. Mass filters (quadrupolar magnets are shown as an example) then separate the different species which are determined by a mass detector. If further information about the reaction intermediates should be obtained, ions passing through mass filter #1 can be fragmented in a collision cell and the resulting ions undergo another separation using mass filter #2 before detection.

Another reason for the limited understanding of active sites is the complexity of most SACs which commonly use inherently inhomogeneous supports like metal oxides with many different adsorption sites where each single-atom site may exhibit dissimilar structure and activity. Recently, we found that atomically dispersed noble metals supported on polyoxometalates (POMs) are active catalysts for hydrogenation and CO oxidation reactions.[11] POMs are considered to be models for metal oxides with structural simplicity, molecularly defined active sites and solubility in polar solvents. Many different classes of inorganic compounds comprising transition metals and POMs have been reported before with applications ranging from medicine[12] and electronic devices[13] to catalysis.[14] Although the Keggin structure of $H_3PW_{12}O_{40}$ has been the earliest reported POM structure,[15] a variety of POMs have been synthesized composed of many different elements and exhibiting very diverse geometries.[16] Keggin-derived lacunary POMs of the type $[PM_{11}O_{39}]^{n-}$ have been among the earliest to be reported, featuring high charge states and high stability. Most transition metal-based complexes comprising POMs have been based on those lacunary POMs with Pd, Rh, or other transition metals.[17] Those serve as excellent homogeneous catalysts predominantly for oxidation reactions or but also enable the in-depth study of reaction mechanisms and active sites in the more commonly used heterogenous POM-based catalysts.[18] As most POMs are symmetric and thus only offer a few discernible sufficiently strong adsorption sites (in some cases only one), they also serve as a platform to investigate reaction mechanisms and parameters governing catalytic activity.[9b] We envisage, that solvent dispersible, POM-supported SAC will be an ideal model system to study the active sites and their dynamics during catalytic reactions using techniques capable of providing structural information with high sensitivity and accuracy, such as mass spectrometry.

Electrospray ionization mass spectrometry (ESI-MS) is based on the formation of an aerosol which is de-solvated and directed by an electric field to yield isolated ions in the gas phase. Due to the mild ionization, intact ions from the liquid phase is separated by a mass filter and analyzed by a detector without fragmentation. In the ionization process, negative

charges are compensated by cations like H^+, Na^+ or K^+. These intact ions can be deliberately separated and fragmented in a controlled manner by accelerating and colliding them with argon atoms. Some of the transferred kinetic energy is used to induce bond breaking and the resulting fragmented ions are further separated and detected (Figure 1). Ion separation allows the identification of very low concentrations of intermediates within a complex reaction mixture, providing information on the exact composition of the molecular structure[19] of the active site including the binding of adsorbates, changes in the support structure[20] as well as the charge state of the metal center and the metal-substrate complex (intermediates).[21] Fragmentation provides further confirmation of the composition, the binding strength of adsorbates as well as the relative stability of intermediates. ESI-MS also provides relative concentrations of intermediates, revealing information on kinetically relevant steps and enabling the quantitative analysis of reaction barriers between intermediates. As we are aware, those advantages of ESI-MS have not been used to investigate SAC systems.

In the present work, we use ESI-MS to study active sites and catalytic reaction mechanisms of POM-supported SACs. During the testing of dozens of metal-POM combinations, we identified three main criteria for the ESI-MS study of stable metal-POM combinations for catalytic reactions. 1. POM-metal mixtures must be completely soluble; 2. POM-metal has to be strongly bonded together in a stoichiometrically defined manner; 3. POM has well-established, reliable synthetic protocol (Figure S1). Based on these criteria, we identified $PW_{11}O_{39}^{7-}$ derived SACs to be the most promising ones for the study. CO and benzyl alcohol oxidation reactions were conducted with SACs based on different metals in the liquid phase. Not only all relevant intermediates hinting at a Mars-van Krevelen mechanism were observed by ESI-MS, but also the rate-limiting step in $PW_{11}O_{39}Rh_1$ catalyzed CO oxidation was determined. Since ESI-MS does not provide direct information on the structure and charge density distribution in the active site, we also employed DFT calculations to confirm the oxidation state changes during the reaction cycle as well as the exact geometry of the experimentally observed intermediates. The POM-based SACs are molecularly well defined with known composition during reaction and are thus ideal systems for DFT calculations. For the liquid phase alcohol oxidation, we determined different reaction mechanisms over $PW_{11}O_{39}Fe_1$ and $PW_{11}O_{39}Pd_1$ catalysts and measured the reaction barriers between different intermediates. This study exemplifies the effectiveness of ESI-MS to examine molecularly defined SACs containing different active metal species in a broad range of reactions.

Results and Discussion

The synthesis of the lacunary POM was performed following a known procedure starting from sodium tungstate.[22] The purity of the sample was confirmed by infrared spectroscopy (Figure S2)[23] by comparison to phosphotungstic acid ($PW_{12}O_{40}$) and sodium tungstate. ^{31}P NMR was further used to verify the absence of P-containing impurities in the POM precursors as well as catalyst samples (Figure S3). As reasoned before, due to their high negative charge, POMs like $PW_{11}O_{39}^{7-}$ are able to bind metal cations strongly although the bonding includes both ionic as well as covalent character. When mixing molar ratios of 1:1 (POM:Rh^{3+}), all the peaks for free $PW_{11}O_{39}$ in the solution disappeared and thus quantitative conversion of $PW_{11}O_{39}$ into $PW_{11}O_{39}Rh_1$ could be assumed (Figure 2a). Rh coordinates to four oxygen in the POM (inset in Figure 2a), as determined by single crystal X-ray crystallography before,[24] and collaborated by DFT calculations. Although varying compositions for $PW_{11}O_{39}Rh_1$ derivatives have been reported including the Cl-containing species, as well as the formation of $PW_{11}O_{39}Rh_2$ or the respective dimeric species $(PW_{11}O_{39}Rh_1)_2$,[17a, 25] these species were not observed by ESI-MS in our system.

We investigated the CO oxidation mechanism for those structurally defined catalysts, using online ESI-MS. When dilute CO was bubbled through a solution of $PW_{11}O_{39}Rh_1$ for 2 min, $\{[Rh(III)_1^{3+}(CO)_2\text{-}(PW_{11}O_{39})^{7-}] + H^+ + K^+\}^{2-}$ (**a-I**, calc.: 1438.54, expt.: 1438.52) with two geminal CO molecules appeared without the reduction of Rh^{3+} (Figure 2b). In contrast, bubbling CO through a solution of $PW_{11}O_{39}$ did not yield mass signals consistent with CO adsorption on the POM (Figure S4). This confirms that the adsorption of CO and its further oxidation is associated with the formation of $PW_{11}O_{39}Rh_1$ as active site.

As mentioned above, the mass-selected intermediates can be fragmented to obtain further information about the composition. At a collision energy of 10 eV, a peak accounting for the desorption of one CO molecule becomes apparent but it seems that the CO oxidation reaction also occurred in the collision cell and species **a-I** was converted into species **a-II** (not observed by ESI-MS) after desorption of the produced CO_2 (Figure 3a and Figure 4). Other peaks were ascribed to a cation exchange reaction in the gas phase as commonly observed during ESI-MS experiments.[26] Reaction of **a-I** at relatively low collision energy indicated that the reaction barrier towards the oxygen vacant species was low. When the solution was treated with CO for 1 h, the previously observed species (**a-I**) disappeared and two species: $\{[Rh(I)_1^+(CO)(CO_2)\text{-}(PW_{11}O_{38})^{5-}] + 2K^+\}^{2-}$ (calc.: 1456.53, expt.: 1456.51) and $\{[Rh(I)_1^+(CO)_2\text{-}(PW_{11}O_{38})^{5-}] + H^+ + K^+\}^{2-}$ (**a-III/a-IV**, calc.: 1432.06, expt.: 1432.07) were formed where one of the oxygen atoms from the support was removed (Figure 2b). This strongly suggested the involvement of a Mars-van Krevelen (MvK) type mechanism with the rapid formation of an oxygen vacancy at room temperature concomitant with the reduction of Rh^{3+} to Rh^+. Although MvK mechanisms have been among the many debated proposed reaction mechanisms for CO oxidation, we present here solid experimental evidence of stoichiometric ratios for atomically precise active sites.

In order to close the catalytic cycle, O_2 was bubbled through the reaction system following 1 h CO treatment. After 1 h, a different species appeared with a composition consistent with $\{[Rh(I)_1^+(CO)_2(O_2)\text{-}(PW_{11}O_{38})^{5-}] + H^+ + Na^+\}^{2-}$ (**a-V**, calc.: 1440.08, expt.: 1440.06) including an O_2 molecule bound to the oxygen vacancy. Fragmentation of that intermediate led to the formation of two species with one or two desorbed CO molecules, respectively. Furthermore, fragmentation also led to the splitting of O_2, and the oxidation and desorption of CO_2 while the oxygen vacancy was refilled and Rh^+ reoxidised. The formed species lost CO to yield $PW_{11}O_{39}Rh_1$ in the gas phase. No desorption of O_2 was observed indicating the strong adsorption of O_2 into the oxygen vacancy (Figure 3b). Bubbling O_2 through a solution containing $PW_{11}O_{39}Rh_1$ without prior reduction by CO did not show O_2 binding on Rh (Figure S5). This further confirms that the oxygen vacancy formation was necessary for strong O_2 binding.

Reoxidation of Rh and refill of the oxygen vacancy did not occur to a significant extent after 1 h although a small but distinguishable new peak was observed (Figure S6a) which we assumed to be the reoxidised species $\{[Rh(III)_1^{3+}(CO)(CO_2)\text{-}(PW_{11}O_{39})^{7-}] + H^+\}^{3-}$ (calc.: 951.38, expt.: 951.39). The low intensity of the peak indicates a high reaction barrier from its predecessor species and a low relative stability compared to the catalyst state after CO_2 desorption. That structure, $\{[Rh(III)_1^{3+}(CO)\text{-}(PW_{11}O_{39})^{7-}] + K^+\}^{3-}$ (**a-VI**, calc.: 951.38, expt.: 951.39), may be observable (Figure S6a) but an overlap with one of the other intermediates formed upon CO bubbling limits the fidelity of the assignment. Either treatments at room temperature for 24 h or at 70 °C for 4 h were necessary for complete catalyst reoxidation and CO desorption in order to regenerate the $PW_{11}O_{39}Rh_1$ species (Figure S6a and b). Overall,

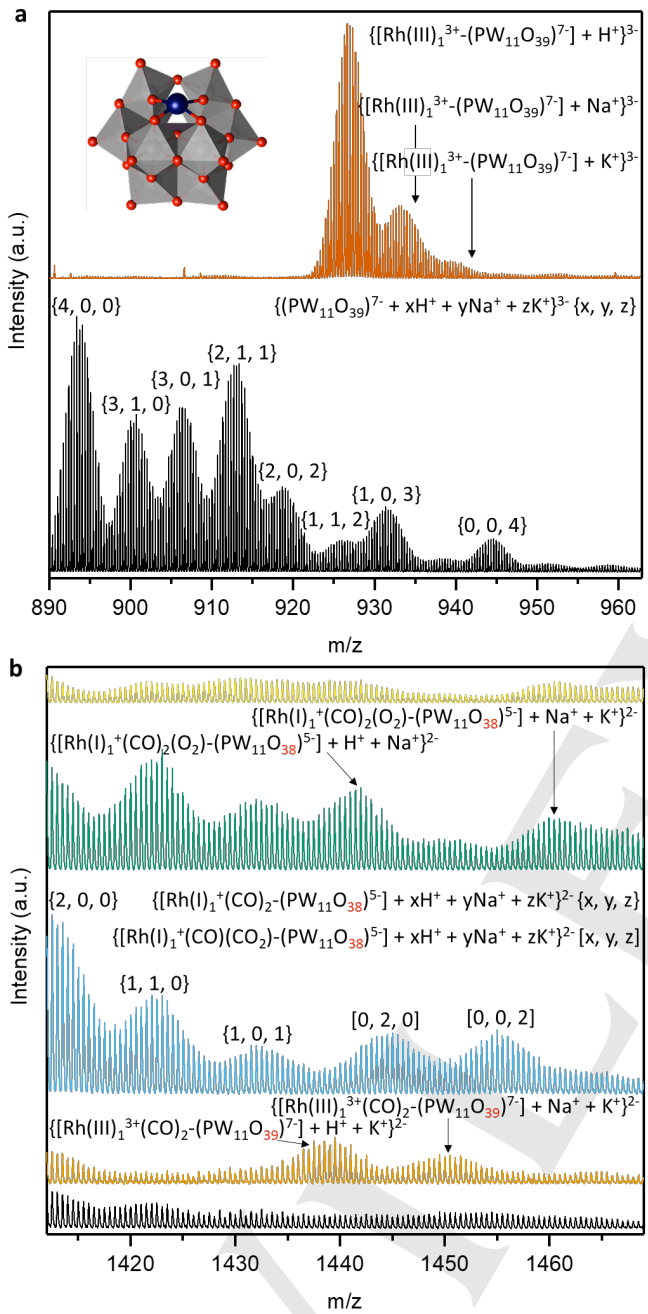

Figure 2. ESI-MS measurements during the CO oxidation reaction on $PW_{11}O_{39}Rh_1$. (a) $PW_{11}O_{39}$ (black) with the respective cation envelope for z=3. $PW_{11}O_{39}Rh_1$ (orange) with a highly reduced cation envelope due to the adsorption of trivalent Rh^{III}. The inset shows the structure of $PW_{11}O_{39}Rh_1$ as determined by single crystal X-ray crystallography before. Since the POM can contain x protons, y sodium and z potassium cations, the following nomenclature will be used in the following for the unequivocal description of ionic species: {x, y, z}. (b) ESI-MS spectra of $PW_{11}O_{39}Rh_1$ after treatment under (black) air, (orange) 2 min CO, (blue) 1 h CO, (green) 1 h CO and subsequently 1 h O_2 and (yellow) 1 h CO and subsequently 24 h O_2. Reactions were carried out in a V_{total} = 0.02 L deionized water with $C_{PW_{11}O_{39}}$ = 0.5 mM and C_{Rh} = 0.5 mM and F_{total} = 100 cm^3 min^{-1} of each gas (5:95 CO:Ar and 5:95 O_2:Ar) at a p_{total} = 1 bar and room temperature. Samples were collected out of the reaction mixture and immediately analysed by ESI-MS.

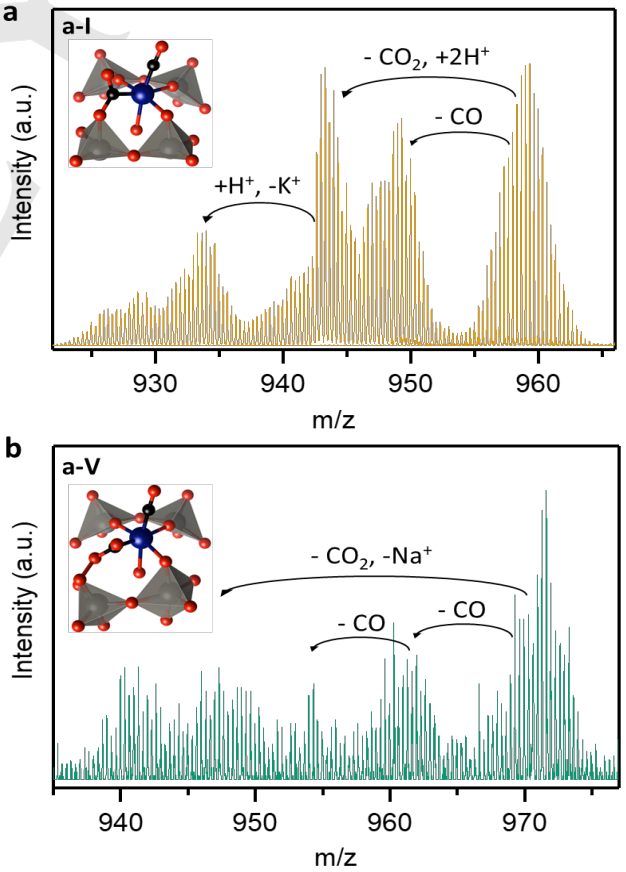

Figure 3. Fragmentation pattern for (a) species **a-I** $\{[Rh(III)_1(CO)_2\text{-}PW_{11}O_{39}^{7-}] + K^+\}^{3-}$ and (b) species **a-V** $\{[Rh(I)_1(CO)_2(O_2)\text{-}PW_{11}O_{38}^{6-}] + Na^+ + K^+\}^{3-}$ at 10 and 6 eV collision energy, respectively. Reaction conditions the same as in Figure 2.

the reaction cycle determined by ESI-MS followed an MvK mechanism with the formation of an oxygen vacancy followed by its refill by O_2. The subsequent splitting of O_2, and oxidation of another CO molecule is rate-determining (Figure 4). The findings obtained for a solubilized SAC, including the overall reaction mechanism and the rate-determining step, matched the results obtained before by combined use of operando XAS, in situ XPS and in situ infrared techniques over the heterogeneous Rh-POM SAC.[9b] Concrete evidence about the reaction stoichiometry and active site composition, which were not available previously, is reported here with less experimental and computational efforts, and without the need for synchrotron facilities. [9b]

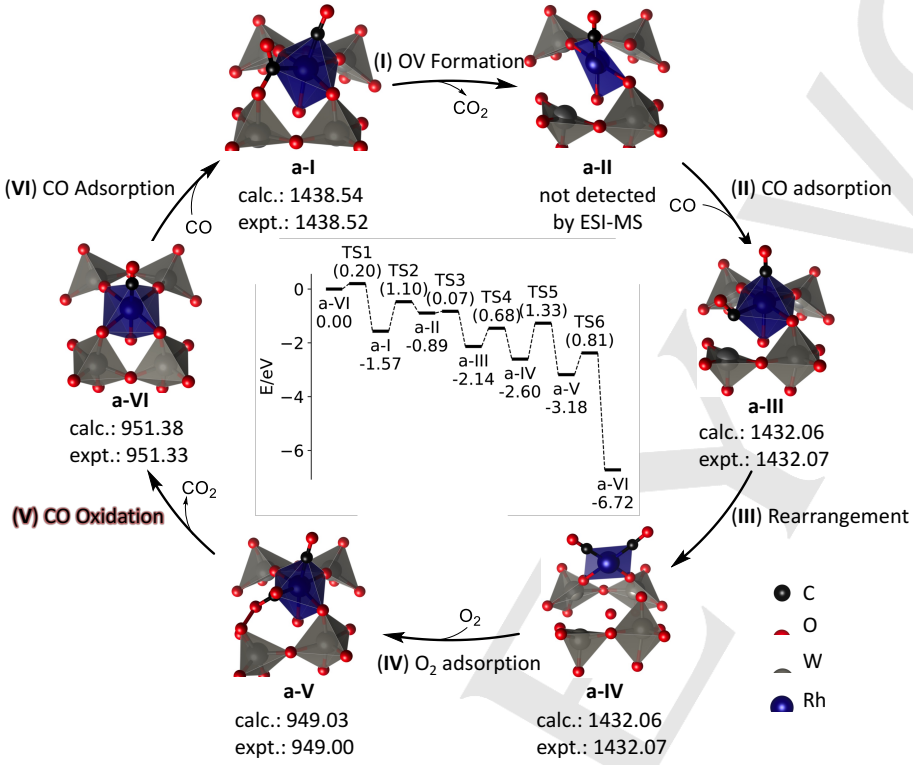

Figure 4. Reaction mechanism of the Rh single-atom catalyzed CO oxidation based on ESI-MS and DFT calculations; the calculated and experimentally determined masses of representative ions are displayed, the rate-determining step is highlighted in red. In the center, the DFT computed energy profile of the CO oxidation reaction is displayed. The numbers in parenthesis are the calculated reaction barriers for each elementary step. In this figure, the $PW_{11}O_{39}$ is simulated by a charged species (4-) in gas phase.

Based on the well-defined catalyst stoichiometries from the MS experiments, we performed DFT calculations to investigate the intermediate structures found by MS as well as the interconnecting reaction barriers. We considered two different models as two limiting cases for the charging state of the catalyst: the first one regards $PW_{11}O_{39}Rh_1$ as isolated, fully deprotonated (charge 4-) species, and the second model considers the impact of counterions (protons) rendering the catalyst system neutral. The results for the charged model are shown in Figure 4 and Figure S8. The first CO adsorption on $PW_{11}O_{39}Rh_1$ is very strong with an adsorption energy of -2.38 eV, compared with the adsorption of O_2 (-0.99 eV) or H_2O molecule (Table S2), producing the stable structure a-VI (Figure 4). The second CO molecule reacts directly with one bridging oxygen forming a carbonate species (**a-I**) through a small barrier (TS1, E_a=0.20 eV). The calculated desorption energy of CO_2 from **a-I** is moderately endothermic (+0.68 eV) with a barrier of 1.10 eV (TS2), creating an O vacancy. Considering the increase of entropy for CO_2 in gas phase, this step will still be exergonic. The intermediate **a-II** is unstable and can transform to **a-III** with a very small barrier (E_a=0.07 eV). This implies that the concentration of **a-II** is very small and may explain why it is not observed in the ESI-MS experiments. Based on a charge density analysis, Rh bound to the lacunary POM is significantly reduced after the formation of the oxygen vacancy consistent with a formal oxidation state change from Rh(III) to Rh(I) (Table S1 and Figure S7) as expected from our previous in situ spectroscopic studies on a comparable Rh SAC.[9b] Concomitant with the reduction of Rh(III), the charge density of the W atom adjacent to the oxygen vacancy is also reduced noticeably. With the change of Rh oxidation state, the ligand structure around Rh rearranges from a slightly distorted octahedron to a square-planar binding mode (**a-IV**). Calculations hence suggest that the active site structure changes during the reaction with alternating binding of Rh to five, four, three or two oxygen atoms of the POM support. From square planar **a-IV**, O_2 adsorbs, both re-oxidizing Rh to 3+ and forcing it into an octahedral environment again. This step is rather difficult with a barrier of 1.33 eV. The last step forms the second CO_2 molecule and regenerates the $PW_{11}O_{39}$ structure in a highly exothermic manner.

Although calculations on this charged model appear to be valid for the investigation of reactions occurring in the gas phase after stripping most of the counterions, the solution structure of the catalyst must be assumed to be different. Therefore, we considered the catalyst structure with protons as counterions in order to neutralize the system. We first optimized 138 structures with different proton locations, and found that protons prefer to occupy the bridging oxygen atoms near the Rh(III) (Figure S9 and Table S2). Starting with this optimal structure, we further analyzed the reaction intermediates as well as the interconnecting transition states. With counterions, most reaction intermediates show similar geometries as their counterparts in the charged model (**a'-I** to **a'-VI** in Figure S10 comparing with **a-I** to **a-VI** in Figure S8). The pathway for the first CO adsorption on **a'-VI**, however, is different: after CO adsorption, **a'-VII** is firstly formed and then it can isomerize to **a'-I** with a small barrier of 0.58 eV, or it directly forms **a'-II** with a barrier of 0.71 eV. Although the isomerization (from **a'-VII** to **a'-I**) is faster, the CO_2 formation (TS'-2) is slower and therefore, the two pathways may co-exist in reactions. In addition, O_2 adsorption is barrierless in

the neutral model (from a'-IV to a'-V) showing a big difference to the charged model (Figure 4 TS5). Finally, the conversion from **a'-II** to **a'-III** is slower than that in the charged model, although the barrier (0.64 eV) is still relatively small. The transition state energy (TS'6) between **a'-V** and **a'-VI** is now the highest (0.89 eV) in the reaction cycle fully consistent with experimental observations that the reaction cycle can be completed at relatively low temperature and that the second CO oxidation step is rate-determining.

After considering the two extreme cases with the catalyst bearing either no counterions or being completely neutralized by protons, it is important to note that the catalyst (de)-protonation should be expected to be fast and highly dynamic throughout the reaction cycle. $PW_{11}O_{39}Rh_1$ may be bound to a varying number of different cations (e.g. H^+, Na^+, or K^+ as observed experimentally). We have demonstrated here that during the ESI-MS measurements, the structures are interconvertible, e.g. the catalyst structure does not change significantly during the ionization procedure.

The selective catalytic oxidation of alcohols using environmentally benign oxidants in water is an important reaction adhering to the principles of green chemistry. Prompted by the widely known oxidation activities of POMs but general lack of mechanistic understanding, we employed ESI-MS to follow the oxidation of benzyl alcohol into benzaldehyde in aqueous hydrogen peroxide over solubilized SACs anchored on $PW_{11}O_{39}$. In catalytic activity tests, TOF values (Table S3) indicate that among the 15 tested metals (Cr, Mn, Fe, Co, Ni, Cu, Zn, Rh, Pd, Ag, Ce, W, Pt, In, and Bi), $PW_{11}O_{39}Fe_1$ seems to be the most relevant candidate regarding its comparably high activity (4.4 h^{-1} at 70 °C) and low price. Conversions were generally kept below 25% to minimize the formation of benzoic acid. Good stability of the catalyst under reaction conditions was confirmed: no obvious decomposition of $PW_{11}O_{39}Fe_1$ species was observed even after reaction at 70 °C for 5 h (Figure S11).

ESI-MS revealed that equimolar mixtures of iron nitrate and POM led to the same active site as observed for $PW_{11}O_{39}Rh_1$ (Figure S12). The addition of benzyl alcohol to solutions containing $PW_{11}O_{39}Fe_1$ led to the formation of the intermediate $[Fe(III)_1^{3+}(C_7H_8O)\text{-}(PW_{11}O_{39})^{7-}]^{4-}$ (**b-I**, calc.: 710.06,

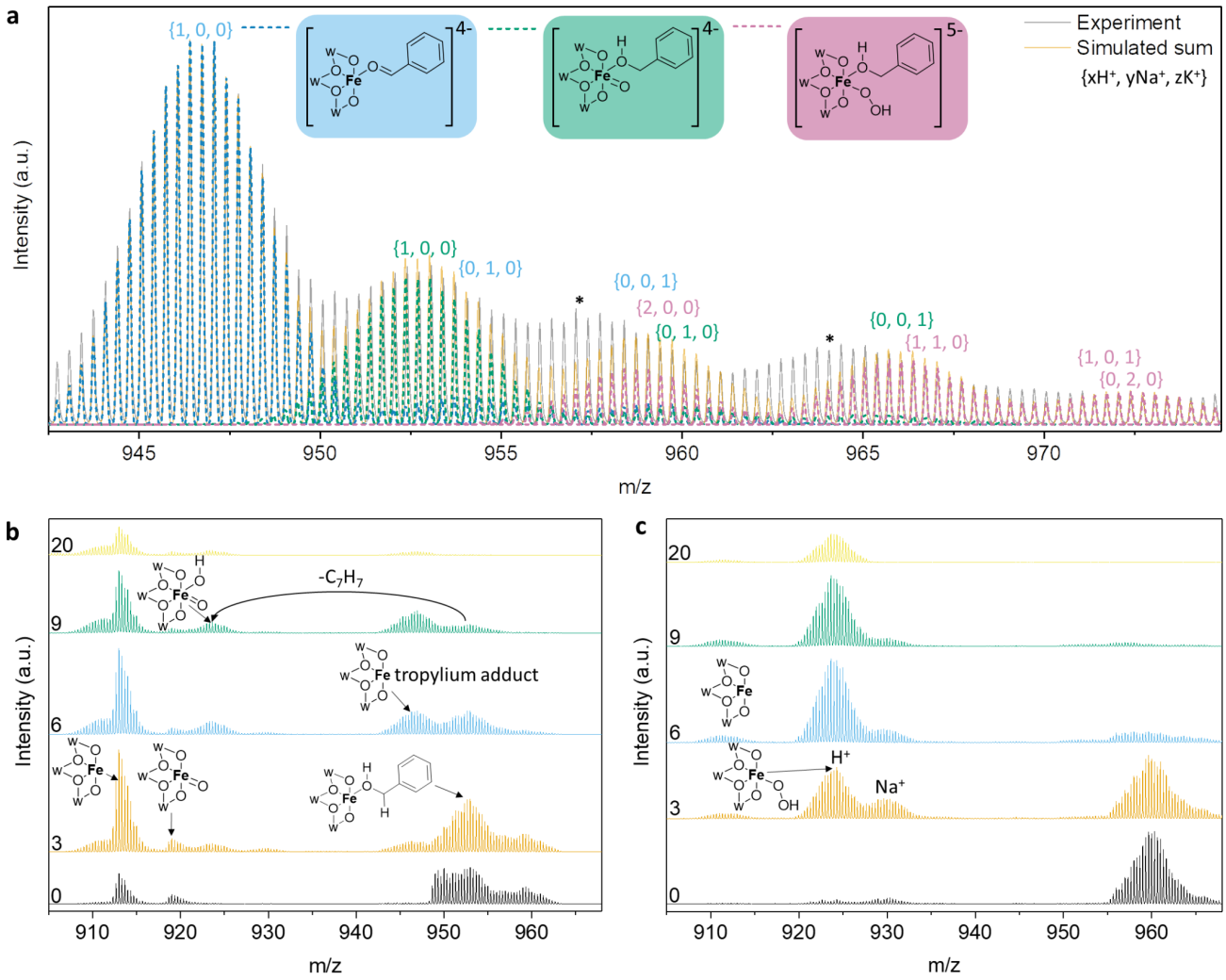

Figure 5. ESI-MS spectra for the $PW_{11}O_{39}Fe_1$-catalysed benzyl alcohol oxidation. (a) Overlap between the experimental spectra during the benzyl alcohol oxidation and a linear combination analysis of three key intermediates during the catalytic cycle. The three observed intermediates carrying different cations $\{xH^+, yNa^+, zK^+\}$ are indicated by different colours at their respective m/z values. Asterisks mark the locations where species occur that are also visible when iron nitrate and $PW_{11}O_{39}$ are mixed (see Figure S11 for more details). Fragmentation pattern for (b) the Fe-oxo (**b-III**) and (c) the Fe-hydroperoxo (**b-II**) intermediates are shown at increasing collision energies (in eV).

expt.: 710.05) (Figure S13) confirming the relatively weak binding of the substrate indicated by the low concentration of the intermediate **b-I** relative to $[Fe(III)_1^{3+}\text{-}(PW_{11}O_{39})^{7-}]^{4-}$ (calc.: 683.30, expt.: 683.28). $PW_{11}O_{39}$ did not adsorb benzyl alcohol (Figure S14) thus providing evidence that the presence of Fe is essential for substrate binding. Other benzyl alcohol derivatives can also be adsorbed on $PW_{11}O_{39}Fe_1$ and give rise to the intermediates $[Fe(III)_1^{3+}(C_7H_7NO_3)\text{-}(PW_{11}O_{39})^{7-}]^{4-}$ (calc.: 721.55, expt.: 721.57) for 4-nitrobenzyl alcohol and $[Fe(III)_1^{3+}(C_8H_{10}O_2)\text{-}(PW_{11}O_{39})^{7-}]^{4-}$ (calc.: 717.56, expt.: 717.57) for 4-methoxybenzyl alcohol. Differences in the adsorption strength of alcohol derivatives seem to follow the order benzyl alcohol < 4-nitrobenzyl alcohol < 4-methoxybenzyl alcohol based on the differences in the concentrations of the alcohol-bound intermediates after liquid phase adsorption (Figure S15).

Upon addition of hydrogen peroxide to the reaction mixture with benzyl alcohol and heating to 90 °C, a range of other species assignable to various reaction intermediates appeared in the ESI-MS spectra (Figure 5a). Although the involvement of high valent Fe-oxo species in catalytic oxidation cycles is frequently reported, little evidence exists about the exact structure and dynamics of active sites even for homogeneous catalysts.[27] In the first step, the alcohol-bound $PW_{11}O_{39}Fe_1$ intermediate **b-I** adsorbed hydrogen peroxide upon removal of a proton, giving rise to intermediate $\{[Fe(III)_1^{3+}(OOH^-)(C_7H_8O)\text{-}(PW_{11}O_{39})^{7-}] + 2H^+\}^{3-}$ (**b-II**, calc.: 958.07, expt. 958.07). At low collision energies of around 3 eV, benzyl alcohol desorbed from **b-II** and a new species with the composition $\{[Fe(III)_1^{3+}(OOH^-)\text{-}(PW_{11}O_{39})^{7-}] + 2H^+\}^{3-}$ (calc.: 922.73, expt. 922.72) formed which was relatively stable against further fragmentation to $PW_{11}O_{39}Fe_1$ (Figure 5b). With the addition of a proton, a water molecule was removed and the Fe(V) oxo species was formed with the composition $\{[Fe(V)_1^{5+}(O^{2-})(C_7H_8O)\text{-}(PW_{11}O_{39})^{7-}] + H^+\}^{3-}$ (**b-III**, calc.: 952.41, expt.: 952.42). The existence and good catalytic oxidation performance of high valence Fe-oxo species on POMs has been proposed computationally and demonstrated experimentally before.[28] Fragmentation pattern of that species are indicative of a much less stable species with decomposition even occurring in the final product, Fe needs to form a transient radical Fe(IV) species **b-IV** which was not observed by ESI-MS presumably due to its low stability. Although the catalyst state binding the product benzaldehyde cannot be easily discerned after short term reaction, ESI-MS analysis of the reaction mixture after 5 h reaction at 70 °C (Figure S16) clearly indicated another peak belonging to $\{[Fe(III)_1^{3+}(C_7H_6O)\text{-}(PW_{11}O_{39})^{7-}] + H^+\}^{3-}$ (b-V, calc.: 947.08, expt.: 947.07). Fragmentation revealed a clean pattern with desorption of benzaldehyde at low fragmentation energies of 2 eV (Figure S17). Excellent overlap between the experimentally measured spectrum and the sum of the predicted isotope pattern was observed (Figure 5a) confirming the presence of all the above-mentioned intermediates. Moreover, a detailed comparison of the experimentally observed and simulated spectra further corroborated the assignment of the intermediates (Figure S18). Combined, we determined a hitherto unknown reaction mechanism for the single atom catalysed oxidation reaction using ESI-MS.

Relative concentrations of various intermediates change as a function of temperature (Figure 6a). Determining those concentrations during catalytic reactions leads to the identification of the temperature dependence of intermediates and thus the activation energy through the Arrhenius equation. Although apparent activation barriers for overall reactions are commonly determined, there is a lack of tools that can easily quantify reaction barriers between intermediates of single-atom

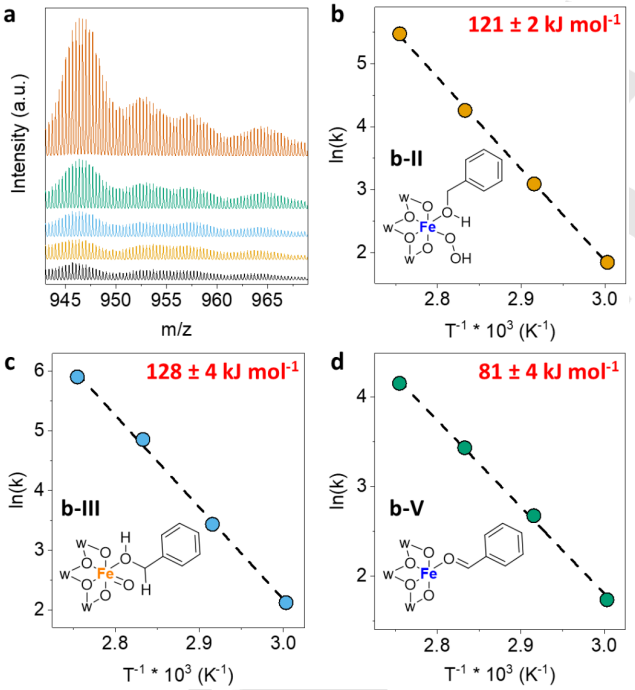

Figure 6. (a) ESI-MS spectra for the $PW_{11}O_{39}Fe_1$-catalysed oxidation reaction at increasing temperatures from bottom to top: 50, 60, 70, 80 and 90 °C. Determination of the reaction barriers for the formation of different intermediates estimated by Arrhenius plots for (b) the Fe-hydroperoxo **b-II**, (c) the Fe-oxo **b-III** and (d) species **b-V** containing benzaldehyde. Reaction conditions for **a-d**: V_{total} = 0.02 L deionized water with $C_{PW_{11}O_{39}}$ = 0.5 mM, C_{Fe} = 0.5 mM, C_{BnzOH} = 25 mM, and $C_{H_2O_2}$ = 50 mM at T = 60 °C – 90 °C under magnetic stirring at 800 rpm. ESI-MS parameters are described in the methods section.

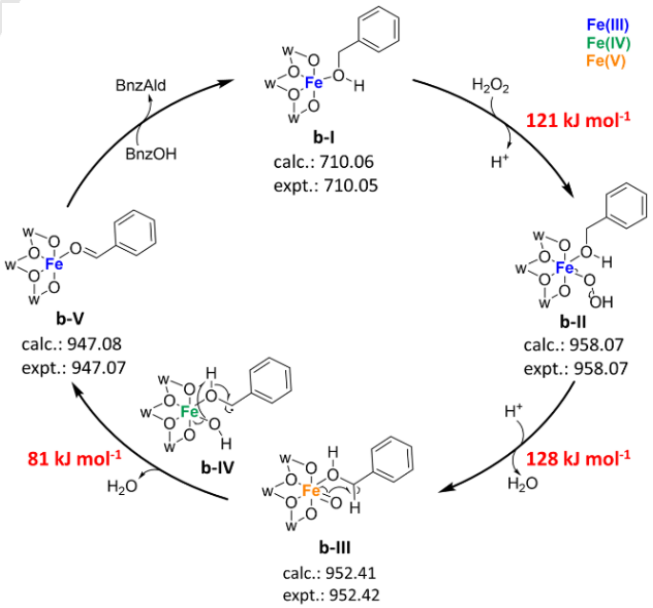

Figure 7. The mechanism of the $PW_{11}O_{39}Fe_1$-catalysed alcohol oxidation reaction is shown. The experimentally determined and simulated masses, as well as the experimentally determined reaction barriers for the most relevant steps are shown. Oxidation states of Fe are indicated by different colours. All of that information was obtained from ESI-MS measurements.

catalysts without computational methods. For all three identified intermediates during $PW_{11}O_{39}Fe_1$-catalysed oxidation reaction, concentrations have been determined at temperatures from 60 to 90 °C (Figure S19). Arrhenius plots (Figure 6b-d) revealed that the activation barriers are 121 ± 2 kJ mol^{-1}, 128 ± 4 kJ mol^{-1} and 81 ± 4 kJ mol^{-1} for the hydroperoxo, the oxo and the benzaldehyde-bound intermediates, respectively. This is consistent with the fact, that for the oxidation reaction of 4-nitrobenzyl alcohol, a less reactive substrate confirmed by previous studies,[29] only reasonable concentrations of the hydroperoxo and 4-nitrobenzaldehyde-containing intermediate were observed while the concentration of oxo intermediate seemed to be negligible (Figure S20). Inversely, the concentration of the oxo species was relatively high when 4-methoxybenzyl alcohol—a more reactive substrate for the alcohol oxidation reaction—was used (Figure S21), indicative of a reduced reaction barrier. The comparably high activation barrier for the Fe-oxo formation is in agreement with the relatively low activity at 70 °C and the previously reported strong pH dependence for the Fe-oxo formation being unfavorable under acidic conditions.[30] For the overall oxidation of organic compounds with Fe-based catalysts involving the formation of Fe-oxo species has been observed to be dependent on the pH with lower values accelerating the reaction. This aligns well with our assumption that the oxo intermediate formation involves the addition of a proton. A decrease in the activity was observed before, however, when the pH dropped to values below 4, presumably due to the inversely pH-dependent hydroperoxo intermediate formation becoming rate-determining.[31] Combining the observed intermediates with the determined activation barriers, we propose a reaction mechanism as shown in Figure 7 where Fe undergoes oxidation state changes involving Fe(III), Fe(IV), and Fe(V), and the formation of the Fe-oxo species is rate-determining.

For a more quantitative correlation between ESI-MS and the catalytic activity of $PW_{11}O_{39}M_1$ in the benzyl alcohol oxidation reaction, we used a methodology proposed by Reek *et al*.[32] They proposed that the catalytic activity can be predicted based on the abundance of the intermediate right before the rate-determining step. In principle, a lower abundance of the species before the rate-determining step would hint at a lower activation barrier and thus higher reactivity. For catalysts following the same reaction mechanism and thus exhibiting the same intermediates, the abundance of the hydroperoxo species was measured during the benzyl alcohol oxidation reaction. Indeed, a good inverse correlation between the abundance of the hydroperoxo species and the turnover frequency was observed (Fig. S 22) further confirming that ESI-MS is a tool to not only determine reaction mechanisms qualitatively but also obtain quantitative information on the catalytic reaction.

SACs based on elements that are located on the right of the so-called oxo-wall[33]—the border between metals forming oxo species and those that do not—are expected to follow a distinct mechanism in the benzyl alcohol oxidation reaction compared with Fe-based SAC. To explore whether ESI-MS is able to differentiate the two, we probed the reaction mechanism of $PW_{11}O_{39}Pd_1$ (Figure S23), which was the most active SAC containing noble metals (TOF = 5 h^{-1} at 70 ˚C, Table S2). During the benzyl alcohol oxidation, distinct intermediates were observed (Figure S24) including the water-containing complex $\{[Pd(II)_1^{2+}(C_7H_8O)(H_2O)\text{-}(PW_{11}O_{39})^{7-}] + 3H^+\}^{2-}$ (**c-II**, calc.: 1456.61, expt.: 1456.56). This complex likely formed from the compound **c-I** which was not observed in the case of benzyl alcohol but only when 4-nitrobenzyl alcohol was used. $PW_{11}O_{39}Pd_1$ then underwent heterolytic cleavage of H_2O_2 to form $\{[Pd(II)_1^{2+}(C_7H_8O)(H_2O)\text{-}(PW_{11}O_{39})^{7-}(OH^-)] + 3H^+ + Na^+\}^{2-}$ (**c-III**, calc.: 1476.61, expt.: 1476.56) probably involving tungsten hydroperoxides that have been described before on POM-based catalysts.[34] The dehydrogenation step of benzyl alcohol then involved a hydride transfer to Pd while the tungsten hydroperoxide was cleaved forming $\{[Pd(II)_1^{2+}(H^-)(C_7H_6O)(H_2O)\text{-}(PW_{11}O_{39})^{7-}] + H^+ + Na^+ + 2K^+\}^{2-}$ (**c-IV**, calc.: 1506.06, expt.: 1506.01). Species **c-II** was presumably reformed by one of those two pathways, either the insertion of O_2 (**c-VI**) and decomposition of the hydroperoxo species,[35] or the deprotonation to **c-VII** and subsequent elimination of water[36] **c-VIII** which would require reoxidation of Pd^0 before the catalytic cycle was closed. The proposed catalytic cycle with all observed intermediates is shown in Figure S25. Reaction with 4-nitrobenzyl alcohol revealed a similar picture with details provided in the Supplementary information (Figure S26). The formation of $PW_{11}O_{39}Pd_1$ dimers in the solid state[17c] has been reported before and based on ESI-MS results, they appear to co-exist with monomeric species in our catalytic system as well. The formation of dimers seems to be concentration-dependent (Figure S27), and the dimer concentration during the benzyl alcohol oxidation reaction can be assumed to be relatively low. Further, DFT calculations suggest that the spontaneous decomposition of $PW_{11}O_{39}Pd_1$ dimers in the presence of weakly coordinating species like water is exothermic by -1.432 eV (Figure S28). Despite this, we cannot completely rule out the contribution of dimeric catalyst species to the overall catalytic activity.

Conclusion

This study exemplifies the advantages of ESI-MS to examine molecularly defined SACs containing different active metal species in solution-phase oxidation reactions. Despite the time passed between injection and analysis, ESI-MS proves effective for the investigation of the structure and structural evolution of solubilized, POM-supported SAC sites during the reaction. Atomically precise active sites with well-defined composition were created and identified, and their dynamics during catalytic cycles were determined. Taking advantage of the soft ionization ability of the electrospray preserving various reaction intermediates, and the high m/z resolution and sensitivity of the mass detector, even low concentrations of unstable intermediates were separated from complex reaction mixtures and analyzed thoroughly. As such, the reaction mechanism, and more importantly the stoichiometry of actives sites as well as key substrate-active site complexes in the full catalytic cycle, were determined for several SACs in both CO and alcohol oxidation. Together with the unique POM-based SACs, this approach is particularly suitable for DFT calculations revealing even further insights into reaction mechanisms.

With the wide variety of POM structures and other soluble metal oxides,[18, 37] as well as the unlimited number of atomically dispersed metals across the periodic table, we believe that this mass spectrometry approach furnishes a general platform for the elucidation of structure-activity correlations of SACs in

solution phase reactions with high precision. Beyond mechanistic analyses, ESI-MS proves powerful in the rapid investigation of large catalyst libraries in minimal amounts of time,[38] while POM-based SACs offer a potent platform for such high-throughput studies in the future.

Acknowledgements

This research is supported by the NUS Flagship Green Energy Program (R-279-000-553-646, and R-279-000-553-731). M. J. H. thanks the SINGA scholarship for supporting his PhD studies. G.S. and P.S. were supported by DOE-BES grant DE-SC0019152. The computational work used the Extreme Science and Engineering Discovery Environment (XSEDE), which is supported by National Science Foundation grant number ACI-1548562. We thank Dr. Bin Zhang for providing some POM samples for this study. We further would like to express our gratitude to the anonymous reviewers who helped improve our manuscript significantly.

Conflict of Interest

The authors declare no conflict of interest.

Keywords: single-atom catalysis • polyoxometalate • mass spectrometry • reaction monitoring • heteropoly acid

[1] a) X.-F. Yang, A. Wang, B. Qiao, J. Li, J. Liu, T. Zhang, *Acc. Chem. Res.* **2013**, *46*, 1740-1748; b) A. Wang, J. Li, T. Zhang, *Nat. Rev. Chem.* **2018**, *2*, 65-81; c) Y. Chen, S. Ji, C. Chen, Q. Peng, D. Wang, Y. Li, *Joule* **2018**, *2*, 1242-1264; d) M. J. Hülsey, J. Zhang, N. Yan, *Adv. Mater.* **2018**, *30*, 1802304; e) S. Ding, M. J. Hülsey, J. Pérez-Ramírez, N. Yan, *Joule* **2019**, *3*, 2897-2929.
[2] a) B. Qiao, A. Wang, X. Yang, L. F. Allard, Z. Jiang, Y. Cui, J. Liu, J. Li, T. Zhang, *Nat. Chem.* **2011**, *3*, 634-641; b) L. DeRita, J. Resasco, S. Dai, A. Boubnov, H. V. Thang, A. S. Hoffman, I. Ro, G. W. Graham, S. R. Bare, G. Pacchioni, X. Pan, P. Christopher, *Nat. Mater.* **2019**, *18*, 746-751; c) L. DeRita, S. Dai, K. Lopez-Zepeda, N. Pham, G. W. Graham, X. Pan, P. Christopher, *J. Am. Chem. Soc.* **2017**, *139*, 14150-14165; d) L. Cao, W. Liu, Q. Luo, R. Yin, B. Wang, J. Weissenrieder, M. Soldemo, H. Yan, Y. Lin, Z. Sun, C. Ma, W. Zhang, S. Chen, H. Wang, Q. Guan, T. Yao, S. Wei, J. Yang, J. Lu, *Nature* **2019**, *565*, 631-635.
[3] a) S. F. J. Hackett, R. M. Brydson, M. H. Gass, I. Harvey, A. D. Newman, K. Wilson, A. F. Lee, *Angew. Chem. Int. Ed.* **2007**, *46*, 8593-8596; b) K. Yamaguchi, K. Mori, T. Mizugaki, K. Ebitani, K. Kaneda, *J. Am. Chem. Soc.* **2000**, *122*, 7144-7145.
[4] a) G. Vilé, D. Albani, M. Nachtegaal, Z. Chen, D. Dontsova, M. Antonietti, N. López, J. Pérez-Ramírez, *Angew. Chem. Int. Ed.* **2015**, *54*, 11265-11269; b) H. Wei, X. Liu, A. Wang, L. Zhang, B. Qiao, X. Yang, Y. Huang, S. Miao, J. Liu, T. Zhang, *Nat. Commun.* **2014**, *5*, 5634; c) P. Liu, Y. Zhao, R. Qin, S. Mo, G. Chen, L. Gu, D. M. Chevrier, P. Zhang, Q. Guo, D. Zang, B. Wu, G. Fu, N. Zheng, *Science* **2016**, *352*, 797-800; d) G. Kyriakou, M. B. Boucher, A. D. Jewell, E. A. Lewis, T. J. Lawton, A. E. Baber, H. L. Tierney, M. Flytzani-Stephanopoulos, E. C. H. Sykes, *Science* **2012**, *335*, 1209-1212; e) F. Huang, Y. Deng, Y. Chen, X. Cai, M. Peng, Z. Jia, P. Ren, D. Xiao, X. Wen, N. Wang, H. Liu, D. Ma, *J. Am. Chem. Soc.* **2018**, *140*, 13142-13146; f) L. Lin, S. Yao, R. Gao, X. Liang, Q. Yu, Y. Deng, J. Liu, M. Peng, Z. Jiang, S. Li, Y.-W. Li, X.-D. Wen, W. Zhou, D. Ma, *Nat. Nanotechnol.* **2019**, *14*, 354-361; g) H. Yan, H. Cheng, H. Yi, Y. Lin, T. Yao, C. Wang, J. Li, S. Wei, J. Lu, *J. Am. Chem. Soc.* **2015**, *137*, 10484-10487; h) S. Ding, Y. Guo, M. J. Hülsey, B. Zhang, H. Asakura, L. Liu, Y. Han, M. Gao, J.-y. Hasegawa, B. Qiao, T. Zhang, N. Yan, *Chem* **2019**, *5*, 3207-3219.
[5] a) J. Zhang, Y. Zhao, X. Guo, C. Chen, C.-L. Dong, R.-S. Liu, C.-P. Han, Y. Li, Y. Gogotsi, G. Wang, *Nat. Catal.* **2018**, *1*, 985-992; b) L. Bai, C.-S. Hsu, D. T. L. Alexander, H. M. Chen, X. Hu, *J. Am. Chem. Soc.* **2019**, *141*, 14190-14199; c) J. Gu, C.-S. Hsu, L. Bai, H. M. Chen, X. Hu, *Science* **2019**, *364*, 1091-1094; d) E. Jung, H. Shin, B.-H. Lee, V. Efremov, S. Lee, H. S. Lee, J. Kim, W. Hooch Antink, S. Park, K.-S. Lee, S.-P. Cho, J. S. Yoo, Y.-E. Sung, T. Hyeon, *Nat. Mater.* **2020**, *19*, 436-442; e) B.-H. Lee, S. Park, M. Kim, A. K. Sinha, S. C. Lee, E. Jung, W. J. Chang, K.-S. Lee, J. H. Kim, S.-P. Cho, H. Kim, K. T. Nam, T. Hyeon, *Nat. Mater.* **2019**, *18*, 620-626.
[6] a) L. Lin, W. Zhou, R. Gao, S. Yao, X. Zhang, W. Xu, S. Zheng, Z. Jiang, Q. Yu, Y.-W. Li, C. Shi, X.-D. Wen, D. Ma, *Nature* **2017**, *544*, 80-83; b) S. Cao, M. Yang, A. O. Elnabawy, A. Trimpalis, S. Li, C. Wang, F. Göltl, Z. Chen, J. Liu, J. Shan, M. Li, T. Haas, K. W. Chapman, S. Lee, L. F. Allard, M. Mavrikakis, M. Flytzani-Stephanopoulos, *Nat. Chem.* **2019**, *11*, 1098-1105; c) J. Xie, R. Jin, A. Li, Y. Bi, Q. Ruan, Y. Deng, Y. Zhang, S. Yao, G. Sankar, D. Ma, J. Tang, *Nat. Catal.* **2018**, *1*, 889-896.
[7] X. Cui, W. Li, P. Ryabchuk, K. Junge, M. Beller, *Nat. Catal.* **2018**, *1*, 385-397.
[8] Y. Tang, C. Asokan, M. Xu, G. W. Graham, X. Pan, P. Christopher, J. Li, P. Sautet, *Nat. Commun.* **2019**, *10*, 4488.
[9] a) Y. Lu, J. Wang, L. Yu, L. Kovarik, X. Zhang, A. S. Hoffman, A. Gallo, S. R. Bare, D. Sokaras, T. Kroll, V. Dagle, H. Xin, A. M. Karim, *Nat. Catal.* **2019**, *2*, 149-156; b) M. J. Hülsey, B. Zhang, Z. Ma, H. Asakura, D. A. Do, W. Chen, T. Tanaka, P. Zhang, Z. Wu, N. Yan, *Nat. Commun.* **2019**, *10*, 1330; c) L. Cao, Q. Luo, W. Liu, Y. Lin, X. Liu, Y. Cao, W. Zhang, Y. Wu, J. Yang, T. Yao, S. Wei, *Nat. Catal.* **2019**, *2*, 134-141.
[10] a) A. J. Therrien, A. J. R. Hensley, M. D. Marcinkowski, R. Zhang, F. R. Lucci, B. Coughlin, A. C. Schilling, J.-S. McEwen, E. C. H. Sykes, *Nat. Catal.* **2018**, *1*, 192-198; b) C. Barroo, Z.-J. Wang, R. Schlögl, M.-G. Willinger, *Nat. Catal.* **2020**, *3*, 30-39.
[11] a) B. Zhang, H. Asakura, J. Zhang, J. Zhang, S. De, N. Yan, *Angew. Chem. Int. Ed.* **2016**, *55*, 8319-8323; b) B. Zhang, G. Sun, S. Ding, H. Asakura, J. Zhang, P. Sautet, N. Yan, *J. Am. Chem. Soc.* **2019**, *141*, 8185-8197.
[12] A. Bijelic, M. Aureliano, A. Rompel, *Angew. Chem. Int. Ed.* **2019**, *58*, 2980-2999.
[13] a) C. Busche, L. Vilà-Nadal, J. Yan, H. N. Miras, D.-L. Long, V. P. Georgiev, A. Asenov, R. H. Pedersen, N. Gadegaard, M. M. Mirza, D. J. Paul, J. M. Poblet, L. Cronin, *Nature* **2014**, *515*, 545-549; b) Z. Zhang, T. Murayama, M. Sadakane, H. Ariga, N. Yasuda, N. Sakaguchi, K. Asakura, W. Ueda, *Nat. Commun.* **2015**, *6*, 7731.
[14] a) D.-L. Long, R. Tsunashima, L. Cronin, *Angew. Chem. Int. Ed.* **2010**, *49*, 1736-1758; b) B. Rausch, M. D. Symes, G. Chisholm, L. Cronin, *Science* **2014**, *345*, 1326-1330.
[15] J. F. Keggin, *Nature* **1933**, *131*, 908-909.
[16] a) P. Yang, U. Kortz, *Acc. Chem. Res.* **2018**, *51*, 1599-1608; b) N. V. Izarova, M. T. Pope, U. Kortz, *Angew. Chem. Int. Ed.* **2012**, *51*, 9492-9510; c) S. Bhattacharya, U. Basu, M. Haouas, P. Su, M. F. Espenship, F. Wang, A. Solé-Daura, D. H. Taffa, M. Wark, J. M. Poblet, J. Laskin, E. Cadot, U. Kortz, *Angew. Chem. Int. Ed.*, *n/a*.
[17] a) X. Wei, R. E. Bachman, M. T. Pope, *J. Am. Chem. Soc.* **1998**, *120*, 10248-10253; b) J. Ettedgui, Y. Diskin-Posner, L. Weiner, R. Neumann, *J. Am. Chem. Soc.* **2011**, *133*, 188-190; c) N. V. Izarova, A. Banerjee, U. Kortz, *Inorg. Chem.* **2011**, *50*, 10379-10386; d) A. Rajan, A. S. Mougharbel, S. Bhattacharya, T. Nisar, V. Wagner, U. Kortz, *Inorg. Chem.* **2020**, *59*, 13042-13049.
[18] a) D. E. Katsoulis, *Chem. Rev.* **1998**, *98*, 359-388; b) S.-S. Wang, G.-Y. Yang, *Chem. Rev.* **2015**, *115*, 4893-4962.
[19] a) T. Chen, Q. Yao, R. R. Nasaruddin, J. Xie, *Angew. Chem. Int. Ed.* **2019**, *58*, 11967-11977; b) Q. Yao, V. Fung, C. Sun, S. Huang, T. Chen, D.-e. Jiang, J. Y. Lee, J. Xie, *Nat. Commun.* **2018**, *9*, 1979; c) C. Sun, N. Mammen, S. Kaappa, P. Yuan, G. Deng, C. Zhao, J. Yan, S. Malola, K. Honkala, H. Häkkinen, B. K. Teo, N. Zheng, *ACS Nano* **2019**, *13*, 5975-5986.
[20] a) S. A. Pelster, R. Kalamajka, W. Schrader, F. Schüth, *Angew. Chem. Int. Ed.* **2007**, *46*, 2299-2302; b) P. Bussian, F. Sobott, B. Brutschy, W. Schrader, F. Schüth, *Angew. Chem. Int. Ed.* **2000**, *39*, 3901-3905; c) B. B. Schaack, W. Schrader, F. Schüth, *Angew. Chem. Int. Ed.* **2008**, *47*, 9092-9095.
[21] a) K. L. Vikse, Z. Ahmadi, C. C. Manning, D. A. Harrington, J. S. McIndoe, *Angew. Chem. Int. Ed.* **2011**, *50*, 8304-8306; b) K. L.

Bamford, S. S. Chitnis, R. L. Stoddard, J. S. McIndoe, N. Burford, *Chem. Sci.* **2016**, *7*, 2544-2552.
[22] R. Contant, *Can. J. Chem.* **1987**, *65*, 568-573.
[23] Y.-k. Miura, H. Imai, T. Yokoi, T. Tatsumi, Y. Kamiya, *Micropor. Mesopor. Mater.* **2013**, *174*, 34-43.
[24] a) V. Artero, D. Laurencin, R. Villanneau, R. Thouvenot, P. Herson, P. Gouzerh, A. Proust, *Inorg. Chem.* **2005**, *44*, 2826-2835; b) X. López, J. J. Carbó, C. Bo, J. M. Poblet, *Chem. Soc. Rev.* **2012**, *41*, 7537-7571.
[25] X. Wei, M. H. Dickman, M. T. Pope, *Inorganic Chemistry* **1997**, *36*, 130-131.
[26] H. Maleki, A. K. Karanji, S. Majuta, M. M. Maurer, S. J. Valentine, *J. Am. Soc. Mass Spectrom.* **2018**, *29*, 230-241.
[27] J. Hohenberger, K. Ray, K. Meyer, *Nat. Commun.* **2012**, *3*, 720.
[28] a) D. Kumar, E. Derat, A. M. Khenkin, R. Neumann, S. Shaik, *J. Am. Chem. Soc.* **2005**, *127*, 17712-17718; b) E. Derat, D. Kumar, R. Neumann, S. Shaik, *Inorg. Chem.* **2006**, *45*, 8655-8663.
[29] M. Ghosh, Y. L. K. Nikhil, B. B. Dhar, S. Sen Gupta, *Inorg. Chem.* **2015**, *54*, 11792-11798.
[30] F. Li, J. England, L. Que, *J. Am. Chem. Soc.* **2010**, *132*, 2134-2135.
[31] H. Lee, H.-J. Lee, D. L. Sedlak, C. Lee, *Chemosphere* **2013**, *92*, 652-658.
[32] J. Wassenaar, E. Jansen, W.-J. van Zeist, F. M. Bickelhaupt, M. A. Siegler, A. L. Spek, J. N. H. Reek, *Nat. Chem.* **2010**, *2*, 417-421.
[33] E. Andris, R. Navrátil, J. Jašík, M. Puri, M. Costas, L. Que, J. Roithová, *J. Am. Chem. Soc.* **2018**, *140*, 14391-14400.
[34] C. Ci, H. Liu, L. Yan, Z. Su, *ChemistryOpen* **2016**, *5*, 470-476.
[35] M. C. Denney, N. A. Smythe, K. L. Cetto, R. A. Kemp, K. I. Goldberg, *J. Am. Chem. Soc.* **2006**, *128*, 2508-2509.
[36] D. Milstein, J. C. Calabrese, I. D. Williams, *J. Am. Chem. Soc.* **1986**, *108*, 6387-6389.
[37] N. I. Gumerova, A. Rompel, *Nat. Rev. Chem.* **2018**, *2*, 0112.
[38] C. A. Müller, C. Markert, A. M. Teichert, A. Pfaltz, *Chem. Commun.* **2009**, 1607-1618.

Entry for the Table of Contents

Insert graphic for Table of Contents here.

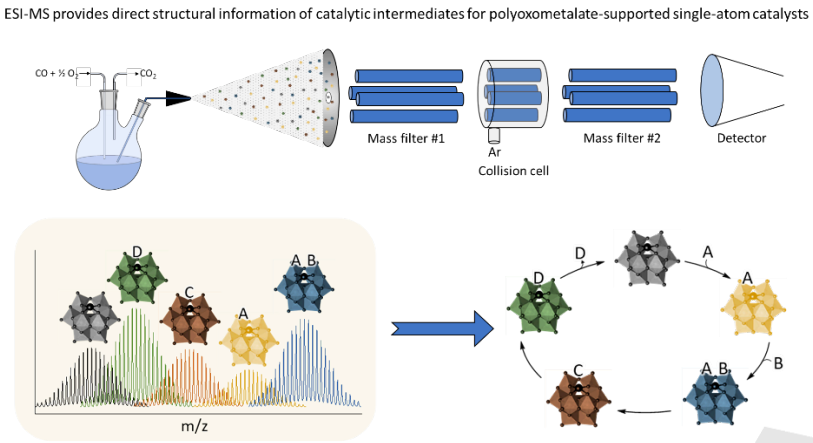

Observing single-atom catalytic sites during reactions: Single-atom catalysts supported on soluble polyoxometalates have been investigated under reaction conditions by electrospray ionisation mass spectrometry. This enables us to observe the exact composition and stoichiometry of active sites as well as their dynamics during CO and alcohol oxidation reactions. Even the apparent activation barriers between intermediates become accessible.

((The Table of Contents text should give readers a short preview of the main theme of the research and results included in the paper to attract their attention into reading the paper in full. The Table of Contents text **should be different from the abstract** and should be no more than 450 characters including spaces.))

Institute and/or researcher Twitter usernames: @nus_che_eng_res; @Ning_Yan_Lab; @MHuelsey